PCCP

Accepted Manuscript

ROYAL SOCIETY OF CHEMISTRY

www.rsc.org/pccp

O_2 Adsorption dependent Photoluminescence Emission from Metal Oxide Nanoparticles

Amir R. Gheisi[1], Chris Neygandhi[1], Andreas K. Sternig[1],

[1] Institute of Particle Technology, Friedrich-Alexander University Erlangen-Nürnberg, Erlangen, Germany

Esther Carrasco[2], Hubertus Marbach[2]

[2] Lehrstuhl für Physikalische Chemie II, Friedrich-Alexander University Erlangen-Nürnberg, Erlangen, Germany

Daniel Thomele[3], Oliver Diwald[3]

[3] Department of Materials Science & Physics, Paris-Lodron University of Salzburg, Salzburg, Austria

Abstract

Optical properties of metal oxide nanoparticles are subject to synthesis related surface defects and impurities. Using photoluminescence spectroscopy and UV diffuse reflectance in conjunction with Auger electron spectroscopic surface analysis we investigated the effect of surface composition and oxygen adsorption on the photoluminescence properties of vapor phase grown ZnO and MgO nanoparticles. On hydroxylated MgO nanoparticles as a reference system, intense photo-luminescence features exclusively originate from surface excitons, the radiative deactivation of which undergoes collisional quenching in O_2 atmosphere. Conversely, on as prepared ZnO nanoparticles a broad yellow emission feature centered at $h\nu_{Em}$ = 2.1 eV exhibits an O_2 induced intensity increase. Attributed to oxygen interstitials as recombination centers this effect originates from adsorbate-induced band bending, which is pertinent to the photoluminescence active region of the nanoparticles. Annealing induced trends in the optical properties of the two prototypical metal oxide nanoparticle systems, ZnO and MgO, are explained by changes in the surface composition and underline that particle surface and interface changes that result from handling and processing of nanoparticles critically affect luminescence.

1. Introduction

Defect engineering belongs to the important challenges in the development of functional particle systems. Moreover, control over defect populations in a particle powder is required in order to endow it with new and desirable properties. Corresponding approaches are particularly demanding since the generation, concentration increase or depletion of defects with functional as well as unwanted properties requires the address along the entire process chain. This spans the wide range beginning with the production of particle powders using a variety of different synthesis routes, to particle processing and integration into the device and, ultimately, to device operation which corresponds to materials exposure to electric current, heat, radiation or mechanical stress.

Motivated by the photoelectronic properties of ZnO nanomaterials and the rich spectrum of related applications, there is a continuously growing number of publications related to the research topic “ZnO nanoparticles and photoluminescence properties”. Recent research activities address the relationship between different defect types and photoluminescence emission features.[1-12] Although it is well established that surfaces and interfaces dominate and control the properties of nanomaterials[13], the chemical and physical nature of ZnO nanoparticles remain unspecified in most cases. Considering the fact that minor changes in synthesis, handling and processing can alter the surface properties of the particles, a particularly unsatisfactory situation is created where an increasing number of publications report discrepant results for the same nanoparticulate material.

In this paper we demonstrate that vapor phase grown ZnO nanoparticles, which were grown under oxygen rich conditions, show bright photoluminescence emission that is

linked to oxygen interstitials in the near surface region. Characteristic adsorbate-induced changes in band bending of semiconducting metal oxides substantially enhance photoluminescence emission in O_2 atmosphere. A powder of ionic MgO nanoparticles with purely surface dependent optical properties, on the other hand, represents a well-suited reference system in order to assess the impact of the nanoparticle surfaces on photoluminescence intensity changes. This study involves a semiconducting and an insulating oxide and underlines the determining influence of sample history and, concomitantly, the nature of the nanoparticle surfaces with regard to their photoluminescence properties. Moreover, it clearly shows that differences in the nature and composition of the surrounding continuous phase, vacuum, gas or solution, may lead to substantial variations in observed photoluminescence intensities.

Bare and well-facetted nanoparticle surfaces that are free from any type of surface adsorbate certainly represent an ideal starting point for related studies. However, required sample activation approaches typically involve high temperature treatment in vacuum. Under such conditions, metal oxide nanomaterials typically undergo substantial particle coarsening and coalescence due to their limited thermal stability. As a result, most nanoparticles deteriorate and transform into ill-shaped microcrystalline materials displaying very complex surface and interface characteristics.[14] The aim of the present study is to document the influence of oxygen in the surrounding continuous phase on the properties of as-synthesized metal oxide particles in comparison to those which were subjected to moderate annealing.

Experimental Section

Material synthesis

For the production of MgO and ZnO nanoparticles we used chemical vapor synthesis (CVS). The details of MgO production technique is given elsewhere. [15,16] ZnO nanoparticle were synthesized by the means of a two-hot-zone CVS reactor (Figure S1, ESI). The reactor system employed for this purpose consists of one quartz glass tube, which is placed inside a heating coil (first zone) followed by a ceramic tube furnace (second zone). The first zone of the tube hosts a ceramic ship with zinc acetate dihydrate powder (≥ 99.0%, Sigma-Aldrich), which is heated to 523 K to sublimate the precursor. An oxygen stream (650 sccm) is mixed with the precursor in the gas phase and transports the metal organic vapor to the second zone of the tube where the furnace provides T = 1073 K inside the glass tube. At this zone, precursor is decomposed and ZnO nanoparticles form as a result of oxidation and homogeneous nucleation in the gas phase. The total pressure (15±2 mbar), as well as flow rate and temperatures in the reactor are kept constant during the time of nanoparticle collection.

Annealing

After production and short contact time with air, the nanoparticle powders were transferred into quartz glass cells, within which thermal sample activation was performed. Annealing treatment is used according to a defined procedure (Figure S2, ESI) for dehydration, dehydroxylation and removal of carbon based surface contaminants. At the beginning, the cell containing nanoparticles powder was evacuated to $p < 10^{-5}$ mbar at room temperature. The respective sample was then heated to 373 K at a rate (r) = 2.5 K min^{-1}, held at this temperature for 15 min (dwell

time, t_d) and then again was evacuated to $p < 10^{-5}$ mbar. Further annealing steps were carried out at p = 650 mbar of oxygen. The powder was stepwise heated in oxygen atmosphere to 473 K (r = 2.5 K min^{-1}, t_d = 15 min) and 673 K (r = 5 K min^{-1}, t_d = 60 min). Before each new annealing step fresh oxygen was added. After each annealing step the sample was cooled to room temperature (cooling time ≈ 30 min) followed by an evacuation to base pressure of $p < 10^{-5}$ mbar in order to remove water and CO_2 as oxidation products (Figure S2, ESI).

Structure and Morphology

X-ray diffraction (XRD) measurements were performed on a Bruker AXS D8 Advance diffractometer using Cu K_α radiation (λ = 154 pm). For transmission electron microscopic measurements with a Phillips CM300 UT TEM operated at 300 kV, small amounts of the metal oxide powders were cast on a carbon grid just by immersing the sample grid into the dry powder.

Spectroscopy

The Auger electron spectroscopy (AES) measurements were performed in a UHV chamber equipped with a Leo Gemini electron column and a hemispherical electron energy analyzer (Omicron Nanotechnology/NanoSAM). During the measurements the base pressure was below $3x10^{-10}$ mbar. Auger spectra were acquired at a primary electron beam energy of 5 kV and a beam current of 3 nA in the constant retardation ratio mode. The AES were acquired in the direct form, i.e. as N vs. E. Three or four surveys are acquired in different areas of each sample. Each spectrum has been taken in a specific area of the surface only once and the beam was blanked

afterwards before moving the sample stage to a different location. A scanned area mode is used for the AES acquisition in order to spread the electron dose (a maximum value of 1.2×10^{-2} C/cm^2 for Mg) over a whole area of 117 x 88 μm^2 and thus to effectively reduce the local electron dose. This procedure guarantees minimization of unwanted electron beam induced effects and to achieve spatially averaged chemical information of the provided samples.[17,18] Apart from the corresponding metal and oxygen elements, carbon was detected in the samples exposed to ambient air. The relative concentrations of each element c_A were obtained by using the following formula:

$$c_A = \frac{\frac{I_A}{S_A}}{\frac{I_A}{S_A} + \frac{I_B}{S_B} + \frac{I_C}{S_C}}$$

where I_A, I_B and I_C correspond to the peak areas for the three elements of interest (O, C, Zn or Mg) or to the peak-to-peak intensities in the derivative spectrum. The selected peaks for the oxides correspond to the main transitions $KL_{2,3}L_{2,3}$ for O and Mg and $L3M_{4,5}M_{4,5}$ for ZnO.[19,20] S_A, S_B and S_C refer to the corresponding sensitivity factors which were taken from reference [21]. For proof of consistency the concentration estimates were derived from both the original spectra (via area analysis) as well as from the correspondingly derived ones (via peak heights). The peak areas were determined via linear background subtraction. The intensities (areas or peak-to-peak heights) of the different elements in each survey were estimated and the corresponding averaged values were determined and used to calculate the concentrations according to the formula given above.

UV diffuse reflectance spectra were acquired at room temperature using quartz glass cells with a Perkin-Elmer Lambda 950 spectrophotometer, equipped with an integrating sphere. The reflectance spectra were converted into absorption spectra using the Kubelka Munk transform procedure. For photoluminescence (PL) measurements, a Fluorolog®-3 Model FL3-22 spectrometer with a continuous wave 450 watt Xenon arc lamp was used for excitation. The double-grating excitation and emission spectrometers of the instrument offer excellent performance in resolution, sensitivity, and stray-light rejection. This system is well-suited for strongly scattering samples such as the nanoparticle powders investigated in this work. PL spectroscopy was performed at room temperature using quartz glass cell that guarantee vacuum condition better than $5 \cdot 10^{-6}$ mbar.

3. Results

3.1. Structure and particle size

ZnO and MgO nanoparticle powders were characterized both directly after synthesis and after controlled annealing at 673 K (Figure S3, ESI). Figure 1 shows representative X-ray diffraction patterns (XRD) for ZnO and reveals that all diffraction peaks are consistent with those of the wurtzite phase. No additional crystalline phases were observed. Annealing of ZnO nanoparticles results in a narrowing of the diffraction features widths, which points to a volume increase of the coherently scattering solid and, therefore, to particle coarsening.

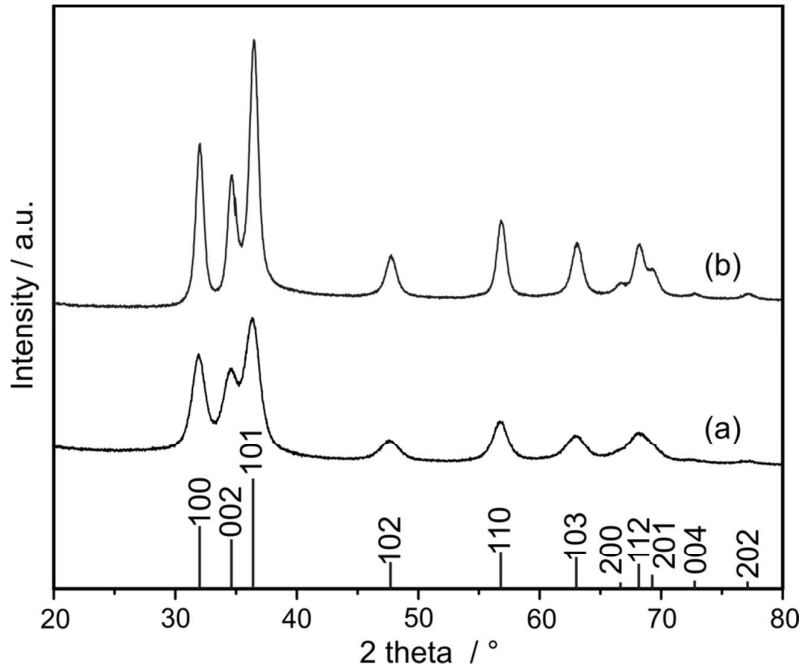

Figure 1: X-ray diffraction patterns of ZnO nanoparticles a) after synthesis; b) after annealing in oxygen (T = 673 K, p = 650 mbar O_2). Vertical lines correspond to the standard XRD pattern of wurtzite ZnO (JCPDS No. 36-1451).

From the full width at the half maximum (FWHM) of the diffraction peaks [22,23] the average crystallite sizes were calculated to be 6 ± 1 nm and 10 ± 1 nm for ZnO after synthesis and after annealing treatment, respectively. (Details of the procedure are found in the ESI)

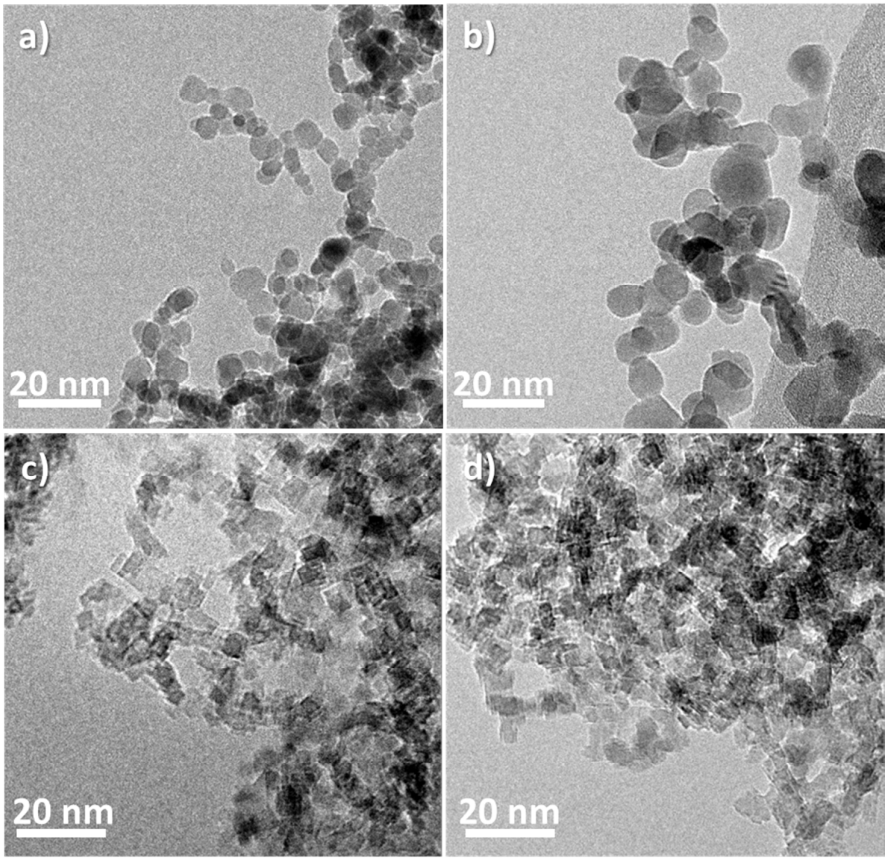

Figure 2: TEM images of a) ZnO nanoparticles after synthesis; b) ZnO nanoparticles after annealing in oxygen (T = 673 K, p = 650 mbar O_2); c) MgO nanoparticles after synthesis and d) MgO nanoparticles after annealing in oxygen (T = 673 K, p = 650 mbar O_2).

Figure 2 shows TEM images of the metal oxide nanoparticles after synthesis (Figures 2a and c) and after annealing (Figures 2b and d). All samples are relatively homogeneous in terms of particle size and shape (see also Figure 3 below). The powders of vapor phase grown nanoparticles can be characterized as ensembles of loosely agglomerated, more (MgO) or less (ZnO) facetted nanoparticles. TEM images also show comparable particle sizes for both types of samples.

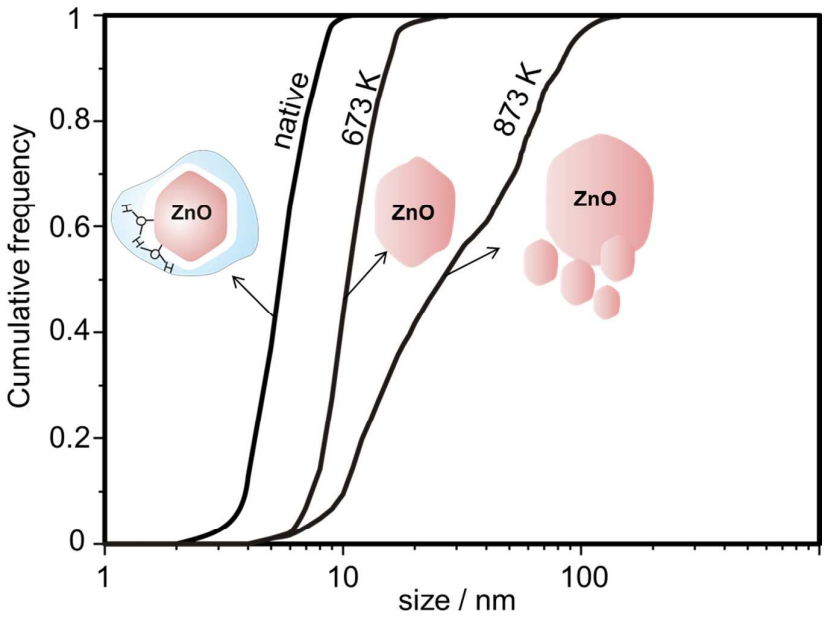

Figure 3: Cumulative particle size distribution plots for ZnO nanoparticles after gas phase synthesis and after annealing to 673 and 873 K in vacuum and dry oxygen atmosphere.

After vacuum annealing at 673 K the particle size distribution in the ZnO nanoparticle powder remains narrow and peaks at an average particle size of 10 nm. This value is perfectly consistent with the average crystallite domain size (see above). MgO nanoparticles, on the other hand, exhibit a higher thermal stability. Their average crystallite domain size of d = 6 ± 1 nm does not change upon annealing (ESI, Figure S4). While MgO is known for its low sinterability even at high temperatures, ZnO exhibits a high sinterability with high grain growth even at lower temperatures. These well-established phenomenon arises from differences in the interface energetics between the two metal oxides.[24] Supply of thermal energy to the metal oxide nanoparticle ensemble initiates ion diffusion and allows the grains to coarsen and to reorganize towards thermodynamic equilibrium. As observed for vapor phase grown

ZnO nanoparticles, annealing temperatures higher than 673 K can induce significant particle size disproportionation effects (Figure 3).[14]

3.2 Surface composition

After vacuum annealing to 673 K and at $p < 10^{-5}$ mbar metal oxide nanoparticles remain partially hydroxylated and may also retain residual surface carbonates or adsorbed CO_2. Previous photoelectron spectroscopy measurements on MgO nanoparticles revealed that – irrespective from vacuum annealing procedures, which were applied ex-situ and prior to the measurement – MgO nanoparticles instantaneously adsorb carbon dioxide and other carbonaceous species from the air.[25] On the highly dispersed MgO with enhanced surface basicity as compared to ZnO this process occurs within a few minutes of exposure to air and the surface contamination level is typically in the range between 20 to 30%. Systematic FT-IR studies on highly dispersed MgO samples reveal that only after vacuum annealing induced desorption at temperatures higher than 873 K, the concentration of hydrogen bonded neighbouring surface OH groups becomes negligibly small.[26-29] Since the present study starts with as-synthesized nanoparticles we expect the coexistence of non-crystalline surface hydroxides, physisorbed water as well as surface hydroxyls. After annealing to 673 K, i.e. above temperature of $Mg(OH)_2$ conversion into MgO, only chemisorbed hydroxyls remain.[26]

The contaminants on ZnO nanoparticle powders mostly originate from the synthesis process, i.e. the thermal decomposition of acetate dihydrate [$Zn(CH_3COO)_2 \cdot 2H_2O$]. [30] Macroscopically, the lightly ochre colour of the as-synthesized ZnO nanoparticle powder (Figure S3, ESI) changes upon annealing to 673 K into white. This change in colour indicates that the organic remnants from the precursor material became decomposed and eliminated during annealing. Attenuated total reflection (ATR) - IR

spectroscopic measurements of ZnO nanoparticle powders in air (spectra shown in Figure S5, ESI) reveal weak absorption related to surface hydroxyls and carboxylates and substantiate this point. A recent FT-IR study on ZnO nanoparticles [31] which were derived from similar precursors materials revealed that IR active and surface adsorbed CO_2 [32,33] exhibit thermal stabilities up to 1073 K.

We characterized the surface composition and stoichiometry of the ZnO nanoparticles with Auger electron spectroscopy in more detail. The estimated concentrations for as-synthesized ZnO nanoparticles as well as for annealed ZnO nanoparticle powders are provided in table 1.

Table 1: Surface composition of ZnO nanoparticles as determined by Auger electron spectroscopy.

Sample	**Relative concentration**		
	Zn	**O**	**C**
ZnO as-synthesized	0,38	0,57	0,05
ZnO annealed	0,43	0,51	0,05

A relative carbon concentration of 0.05 was found in both cases. The results in table 1 suggest that the oxygen content exceeds that of Zn in both samples and is higher in the as-synthesized sample. Comparison of the Auger spectra (not shown) with those in literature reveal a good agreement in energy and position of the respective features. For a reliable determination of the ZnO nanoparticles' stoichiometry we used the atomic ratio of O to Zn (i.e. the ratio of O intensity to Zn intensity corrected by their respective sensitivity factors, $\frac{\frac{I_O}{S_O}}{\frac{I_{Zn}}{S_{Zn}}}$) and compared these values with data

reported for different faces of atomically clean ZnO single crystals [34] (Table S1, ESI). As a conclusion, the annealed ZnO nanoparticle samples were found to correspond to a stoichiometric compound, while the as-synthesized ZnO contains excess oxygen above the stoichiometric composition.

3.3 Optical Properties

UV-Vis Diffuse Reflectance Spectroscopy

Before as well as after annealing the MgO nanoparticle powders adopt a white slightly bluish opalescent colour. The related UV-Vis Diffuse Reflectance spectra show absorption features at energies above 5.0 eV and 5.4 eV for vacuum annealed and as-synthesized MgO nanoparticle powders, respectively. The shift in the absorption threshold is attributed to the annealing induced transformation of photoluminescence inactive surface hydroxides - present on the as-synthesized nanoparticle sample - into the oxide as well as to the desorption of surface adsorbed water from the particle surface. A fraction of low coordinated surface elements become uncovered and addressable by light excitation with sub band gap energy.[35]

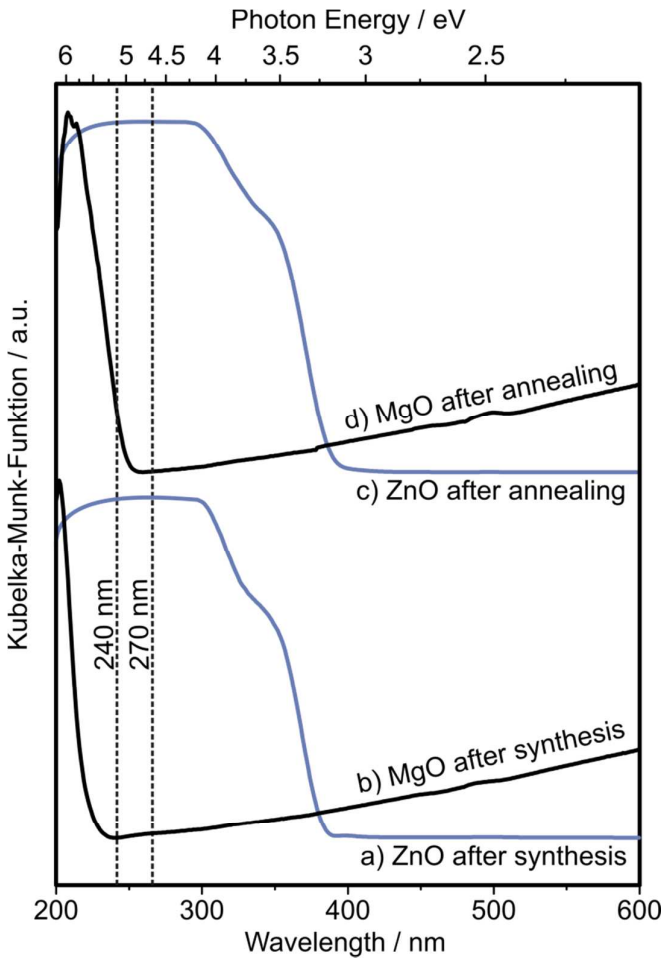

Figure 4: UV-Vis Diffuse Reflectance spectra of a) ZnO after synthesis; b) MgO after synthesis; c) ZnO after annealing in oxygen (T = 673 K, p = 650 mbar O_2); d) MgO after annealing in oxygen (T = 673 K, p = 650 mbar O_2). The spectra were acquired at T = 298 K and in the presence of 10 mbar O_2 in order to omit luminescence effects. The dashed vertical lines indicate the excitation energies selected for the photoluminescence emission measurements.

In comparison to MgO as an insulator - the band gap E = 7.8 eV corresponds to a wavelength below λ = 200 nm - the band gap of ZnO (E = 3.4 eV) corresponds to the absorption threshold at $\lambda \sim$ 370 nm and is clearly observable in the spectra of ZnO (Figure 4a after synthesis and Figure 4c after annealing).

Photoluminescence Spectroscopy

We chose the excitation energies for the two metal oxides on the basis of the most intense PL emission intensities and used hv_{Exc} = 4.6 eV (λ_{Exc} = 270 nm) as an excitation energy for ZnO and hv_{Exc} = 5.2 eV (λ_{Exc} = 240 nm) as an excitation energy for MgO (Figure 4). Whereas the respective excitation energy for ZnO exceeds the optical band gap, the 5.2 eV excitation light used for MgO exclusively addresses localized defect states related to coordinatively unsaturated surface ions or interfaces.[16,36-39]

Figure 5 compares the PL emission spectra obtained on ZnO in the vacuum ($p < 10^{-5}$) and in oxygen atmosphere (p = 10 mbar O_2). Figure 5a corresponds to a ZnO powder sample after synthesis. Spectrum acquisition in vacuum reveals a weak UV luminescence band centered at hv_{Em} = 3.3 eV (λ_{Em} = 376 nm).

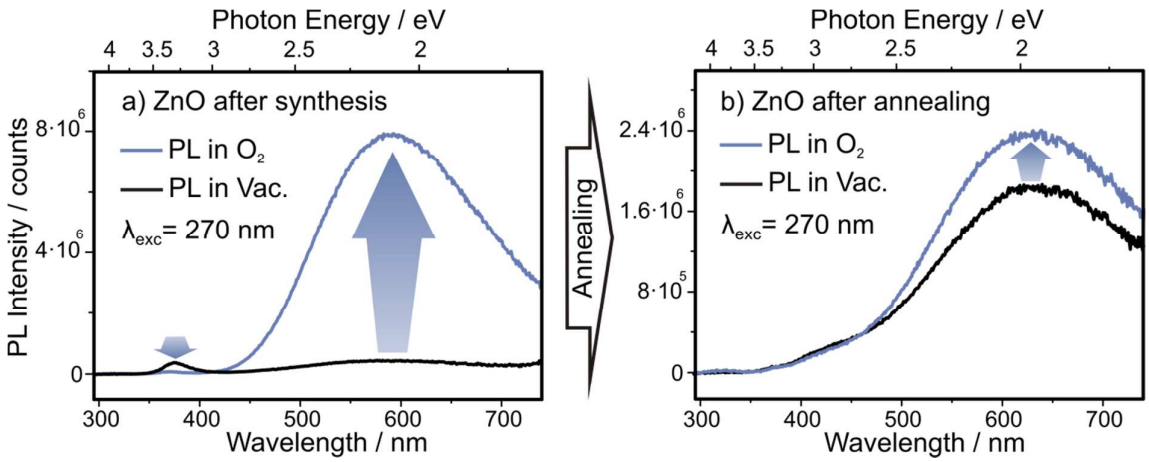

Figure 5: Photoluminescence (PL) spectra of **a)** ZnO after synthesis; **b)** ZnO after annealing in oxygen (T = 673 K, p = 650 mbar O_2); Upon excitation at hv_{Exc} = 4.6 eV, the respective PL emission spectra are recorded either in vacuum ($p < 10^{-5}$ mbar) or in O_2 atmosphere (10 mbar) at T= 298 K.

In addition, there is a broad emission feature with a maximum at hv_{Em} = 2.1 eV (λ_{Em} = 590 nm) and of only small intensity. In oxygen atmosphere the intensity is enhanced, while the band in the UV region becomes completely extinguished. Figure 5b shows the spectra for annealed ZnO nanoparticles. Both spectra - irrespective from whether they were acquired in vacuum or in oxygen atmosphere - do not show any UV emission band. In comparison to the as-synthesized sample, they show a red-shifted visible band centered at hv_{Em} = 2 eV (λ_{Em} = 630 nm) of by a factor of 3-4 reduced intensity.

As the MgO nanoparticles have been subjected to the same annealing procedure, their surfaces remain hydroxylated. Despite the fact that after synthesis most coordinatively unsaturated surface elements remain covered by adsorbates, the respective particle system already shows substantial photoluminescence (Figure 6a), such as the band centered at hv_{Em} = 3.2 eV (λ_{em} = 390 nm).

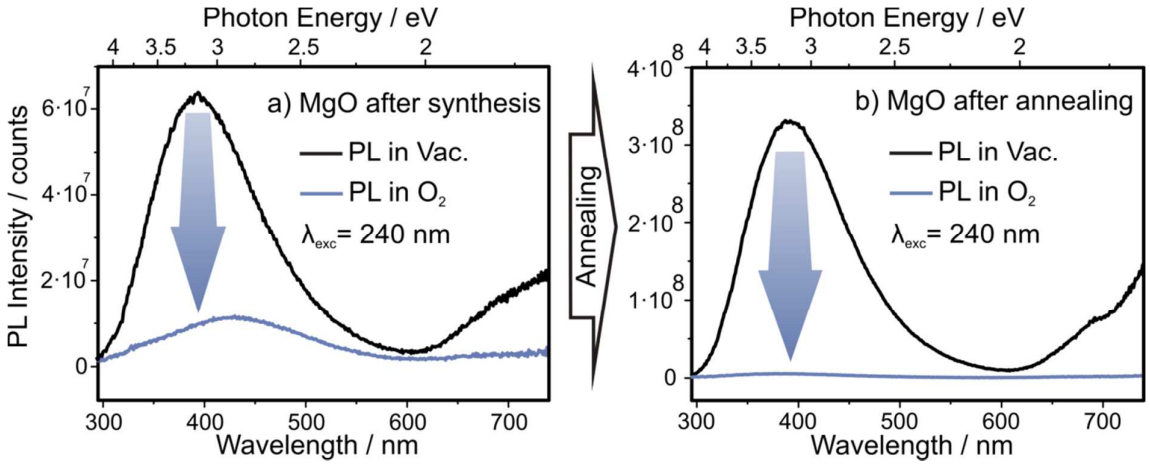

Figure 6: Photoluminescence (PL) spectra of **a)** MgO nanoparticles after synthesis; **b)** MgO nanoparticles after annealing in oxygen (T = 673 K, p = 650 mbar O_2).

Samples are excited at $h\nu_{Exc}$ = 5.2 eV and acquired at T= 298 K either in vacuum (black line, $p < 10^{-5}$ mbar) or in O_2 atmosphere (blue line, 10 mbar).

Vacuum annealing at 673K leads to an intensity enhancement by a factor of about five. In contrast to the PL emission effects observed for ZnO, the MgO related bands are perfectly quenched in the presence of gaseous oxygen (see blue in Figure 6).

4. Discussion

The effect of O_2 adsorption on the photoluminescence (PL) emission properties of two prototypical metal oxides with high and comparable surface-to-volume ratios is in the focus of this study. As a first important conclusion, the nature of the surrounding gasphase has a substantial effect on the photoexcited states formed inside a nanoparticle powder. Moreover, oxygen adsorption effects can disclose valuable information about the location of underlying defects.[40,41] Table 2 summarizes the two opposite trends observed for O_2 adsorption on the PL emission intensity of insulating MgO nanoparticles, on the one hand, and semiconducting ZnO nanoparticles, on the other hand.

Table 2: O_2 pressure dependent photoluminescence emission trends in metal oxide nanoparticle systems.

	$h\nu_{Exc}$ / eV	$h\nu_{Em}$/ eV	Intensity change with O_2 partial pressure	References
ZnO	4.6	2.1	↑	this study
MgO	5.2	3.2	↓	Ref 16

The ZnO photoluminescence emission at hv_{Em} = 2.1 eV (λ = 600 nm) corresponds to yellow light and - when observed on ZnO nanostructures - is attributed to deep trap states related to oxygen interstitials.[3,11,42-43] DFT stability diagrams indicate that oxygen interstitials represent stable defects in ZnO structures in oxygen rich conditions.[4,43] A recent STM luminescence spectroscopy study on atomically clean ZnO thin films[11] has revealed that an emission feature at hv_{Em} = 2.1 eV (λ = 595 nm) is subject to the growth conditions in the excess of atomic oxygen.

We observe a positive PL intensity dependence on the presence of gaseous oxygen (Figure 5a). The O_2 adsorption effect proves the underlying defect's location in the near surface region, i.e. in the range of the depletion layer of the semiconductor particle, where adsorbate induced surface potential changes and band bending become active [41]. While molecular oxygen acts for surface excited states of MgO as a photoluminescence quencher (see below), the absence of PL quenching in case of ZnO nanoparticles rules out that the underlying excitonic transition is localized at distinct defects direct at the nanoparticle surface.

Materials specific issues need to be included into the discussion of the optical ZnO nanoparticle properties: the PL emission effect is strongest on the as-synthesized sample derived from the thermal decomposition of Zn acetate dihydrate.[31] On such samples, AES analysis points to a surface contamination with carbon that roughly corresponds to 5% (Table 1). As the nanoparticles emerge from the oxidative decomposition of an oxygen rich Zn precursor, we assume that they exhibit a surplus in oxygen. Taking into account the measurement uncertainty of the quantitative

Auger analysis, the as-synthesized ZnO particles are in fact enriched in oxygen above the stoichiometric composition (Table S1, ESI), whereas those which - prior to the AES analysis - had been annealed to 673 K - correspond to a stoichiometric compound. The oxygen excess may also stem from oxygen containing adsorbates such as surface carbonates or carboxylates. The photoluminescence fingerprint, i.e. the emission band in the yellow light range, however, points to oxygen interstitials inside the lattice of the vapor phase grown nanoparticles. Annealing to 673 K initiates particle coarsening and, concomitantly, leads to crystallite domain size increase from 6 ± 1 nm to 10 ± 1 nm (Figures 2 and 3). This reveals that ion mobility and mass transfer are significant at these temperatures. We therefore attribute the PL emission intensity decrease in Figure 5b to the thermally induced annihilation of growth related lattice interstitials. MgO nanoparticles are completely different in this respect. As an ionic insulator and a nonreducible metal oxide we can expect a stoichiometric compound exhibiting a substantially higher thermal stability with regard to sintering and in comparison to ZnO (Figures 1-3, S2)

In ZnO photogenerated electrons and holes either recombine radiatively by a direct band-to-band recombination mechanism producing the UV emission band (Figure 5a) or via a trap assisted mechanism upon emission of photons having less energy than the optical band gap.

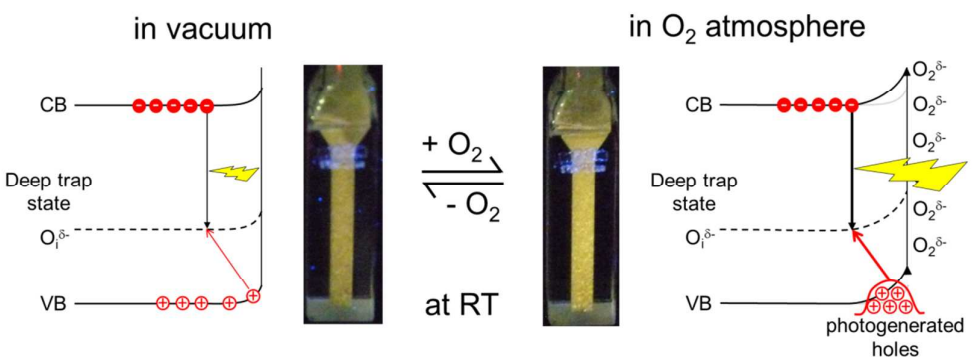

Figure 7: Schematics of the energy band diagram (not to scale) for ZnO nanoparticles after synthesis containing oxygen interstitials. The vertical arrows in downward direction depict the radiative recombination process which produces the PL emission band at 2.1 eV (λ = 600 nm, Figure 5). O_2 adsorption (right panel) enhances surface band bending and drives photogenerated holes into the surface near region. Subsequent hole trapping by deep trap states such as oxygen interstitials $O_i^{\delta-}$ enforces trap assisted recombination and yields yellow photoluminescence emission.

The effect of oxygen on the intensity of ZnO nanoparticles can be consistently explained by band bending on ionic semiconductors.[41] Adsorption of respective acceptor molecules (Figure 7) enhances surface band bending and drives photogenerated holes into the surface near region.[42] We suggest that subsequent hole trapping at oxygen interstitials as deep trap states enforces their recombination with photogenerated electrons yielding the yellow photoluminescence emission.

For powders of entirely dehydroxylated MgO nanocubes, it is well-established that two absorption bands - far below the bulk absorption threshold of MgO (7.8 eV) - are associated with corner (4.6 eV) and edge sites (5.2 eV).[39] In addition, two closely spaced photoemission bands at 3.2 eV and 3.4 eV that are linked to the photoexcitation of corners and edges, respectively.[44,45] As an entirely new insight from this study, hydroxylated MgO particle systems, which were investigated right after synthesis and prior to any activation treatment in vacuum show appreciable surface dependent photoluminescence. Consistent with the effect of hydroxyls on the electronic structure of MgO surface elements [46], the respective emission feature with a maximum at $h\nu_{Em}$ = 3.2 eV is red-shifted in comparison to those observed on adsorbate free particle surfaces. While in case of ZnO where the PL emission

originating from surface near region is only indirectly affected by the adsorption of electron acceptors or donors, the excitonic properties of MgO nanoparticles involve localized excited states and are exclusively surface related.

The ZnO precursor used for this study, i.e. $Zn(CH_3COO)_2 \cdot 2H_2O$, is widely employed for ZnO nanoparticle synthesis in the gas phase as well as in solution.[47-53] The majority of these studies lack information on synthesis related remnants and their potential influence on the optical materials properties. This study also involves a detailed AES analysis and shows that at least a surface fraction of 5% related adsorbates survives high vacuum treatment at 673 K. While these contaminants do not seem to affect the properties of the photoluminescing nanoparticles, molecular oxygen in the gas phase does. It must be concluded that every change in its sticking properties as well as in its concentration in the surrounding continuous phase critically affects the photoluminescence emission yield, irrespective of whether the surface excited state is directly located at the surface (MgO) or in the depletion layer underneath the surface of the semiconductor (ZnO).

Photoluminescence is a well-suited spectroscopic technique to perform adsorption studies on semiconducting metal oxide particle systems.[54-56] Thus, a systematic investigation of synthesis related additives and contaminants belongs to the characterization challenges associated with the identification of defects and other materials specific factors that determine the photoelectronic properties of ZnO nanostructures. Irrespective of whether one deals with semiconducting or insulating metal oxide nanoparticles, a reliable discussion of their photoluminescence properties always requires to address nature and composition of the particle interfaces as well as composition of the surrounding continuous phase. This is

particularly important for defect engineering and for the stabilization of derived functional properties in nanomaterials where synthesis and processing matters.

Conclusions

This work compares the photoluminescence of two prototypical metal oxide nanoparticles systems with identical surface-to-volume ratios, ZnO as an ionic semiconductor and MgO as an ionic insulator. As inferred from Auger electron analysis and photoluminescence emission, the growth of ZnO nanoparticles under oxygen rich conditions generates oxygen interstitials which act as deep traps and assist radiative charge carrier recombination upon emission of yellow light ($h\nu_{Em}$ = 2.1 eV). The presence of oxygen in the surrounding continuous phase was found to have a critical and – for the two metal oxides – opposite influence on the measured photoluminescence intensities. While it quenches photoemission from surface excited states on MgO nanoparticles, it substantially enhances the emission intensity on ZnO because of adsorbate-induced band bending across the semiconductor interface. This study underlines that resolving controversies in the reported optical properties of technically relevant metal oxide nanoparticles requires a more complete documentation of structural and compositional properties of bulk and surface and – in particular – the address of their photoelectronically interactive surfaces.

Acknowledgments

We acknowledge support from the Deutsche Forschungsgemeinschaft project DI 1613/2-1 as well as support in the framework of COST Action (CM1104) “Reducible oxide chemistry, structure and functions”. H.M. and E. C. acknowledge support by DFG through grant MA 4246/1-2, research unit FOR 1878/ funCOS and the Excellence Cluster “Engineering of Advanced Materials” granted to the FAU Erlangen-Nürnberg. This work was also conducted within the framework of the COST Action CM1301 (CELINA).

References

1 A. van Dijken, E. A. Meulenkamp, D. Vanmaekelbergh and A. Meijerink, *Journal of Luminescence*, 2000, **90**, 123–128.
2 V. Ischenko, S. Polarz, D. Grote, V. Stavarache, K. Fink and M. Driess, *Adv. Funct. Mater.*, 2005, **15**, 1945–1954.
3 A. B. Djurišić and Y. H. Leung, *Small*, 2006, **2**, 944–961.
4 A. Janotti and C. G. van de Walle, *Phys. Rev. B*, 2007, **76**.
5 G. Brauer, W. Anwand, D. Grambole, W. Egger, P. Sperr, I. Beinik, L. Wang, C. Teichert, J. Kuriplach, J. Lang, S. Zviagin, E. Cizmar, C. C. Ling, Y. F. Hsu, Y. Y. Xi, X. Chen, A. B. Djurisic and W. Skorupa, *Phys. Status Solidi (c)*, 2009, **6**, 2556–2560.
6 D. Wang, Z. Q. Chen, D. D. Wang, N. Qi, J. Gong, C. Y. Cao and Z. Tang, *Journal of Applied Physics*, 2010, **107**, 023524.
7 C. Klingshirn, J. Fallert, H. Zhou, J. Sartor, C. Thiele, F. Maier-Flaig, D. Schneider and H. Kalt, *phys. stat. sol. (b)*, 2010, **247**, 1424–1447.
8 K. E. Knutsen, A. Galeckas, A. Zubiaga, F. Tuomisto, G. C. Farlow, B. G. Svensson and A. Y. Kuznetsov, *Physical Review B - Condensed Matter and Materials Physics*, 2012, **86**, 121203(R).
9 H. Zhang, A. R. Gheisi, A. Sternig, K. Muüller, M. Schowalter, A. Rosenauer, O. Diwald and L. Maüdler, *ACS Applied Materials and Interfaces*, 2012, **4**, 2490–2497.
10 C. Drouilly, J.-M. Krafft, F. Averseng, H. Lauron-Pernot, D. Bazer-Bachi, C. Chizallet, V. Lecocq and G. Costentin, *Applied Catalysis A: General*, 2013, **453**, 121–129.
11 F. Stavale, N. Nilius and H.-J. Freund, *Journal of Physical Chemistry Letters*, 2013, **4**, 3972–3976.

12 F. Stavale, L. Pascua, N. Nilius and H.-J. Freund, *J. Phys. Chem. C*, 2014, 13693–13696.
13 D. R. Baer, M. H. Engelhard, G. E. Johnson, J. Laskin, J. Lai, K. Mueller, P. Munusamy, S. Thevuthasan, H. Wang, N. Washton, A. Elder, B. L. Baisch, A. Karakoti, Kuchibhatla, Satyanarayana V. N. T. and D. Moon, *J. Vac. Sci. Technol. A*, 2013, **31**, 50820.
14 Springer Series in Surface Science, ed., *Defects on Oxide Surfaces,* T. Berger, O. Diwald, *Defects in Particle Systems,* 2015.
15 E. Knözinger, O. Diwald and M. Sterrer, *Journal of Molecular Catalysis A: Chemical*, 2000, **162**, 83–95.
16 N. Siedl, D. Koller, A. K. Sternig, D. Thomele and O. Diwald, *Phys Chem Chem Phys*, 2014, **16**, 8339–8345.
17 M.-M. Walz, F. Vollnhals, M. Schirmer, H.-P. Steinrück and H. Marbach, *Phys. Chem. Chem. Phys*, 2011, **13**, 17333.
18 A. Vittadini, M. Schirmer, M.-M. Walz, F. Vollnhals, T. Lukasczyk, H.-P. Steinrück, H. Marbach, A. Riss, M. J. Elser, B. Schürer and O. Diwald, *Langmuir*, 2012, **28**, 7851–7858.
19 P. Bassett, T. Gallon, M. Prutton and J. Matthew, *Surface Science*, 1972, **33**, 213–218.
20 J. Onsgaard, S. M. Barlow and T. E. Gallon, *J. Phys. C: Solid State Phys.*, 1979, **12**, 925–942.
21 S. Mroczkowski and D. Lichtmann, *J. Vac. Sci. Technol. A*, 1985, **3**, 1860.
22 C. Weidenthaler, *Nanoscale*, 2011, **3**, 792–810.
23 A. Weibel, R. Bouchet, F. Boulc' and P. Knauth, *Chem. Mater.*, 2005, **17**, 2378–2385.
24 R. H. R. Castro, R. B. Tôrres, G. J. Pereira and D. Gouvêa, *Chem. Mater.*, 2010, **22**, 2502–2509.
25 A. Sternig, O. Diwald, S. Gross and P. V. Sushko, *Journal of Physical Chemistry C*, 2013, **117**, 7727–7735.
26 E. Knözinger, K.-H. Jacob, S. Singh and P. Hofmann, *Surface Science*, 1993, **290**, 388–402.
27 O. Diwald, M. Sterrer and E. Knözinger, *Physical Chemistry Chemical Physics*, 2002, **4**, 2811–2817.
28 C. Chizallet, H. Petitjean, G. Costentin, H. Lauron-Pernot, J. Maquet, C. Bonhomme and M. Che, *Journal of Catalysis*, 2009, **268**, 175–179.
29 C. Chizallet, G. Costentin, H. Lauron-Pernot, J. M. Krafft, P. Bazin, J. Saussey, F. Delbecq, P. Saufet and M. Che, *Oil and Gas Science and Technology*, 2006, **61**, 479–488.
30 This is reasoned by the fact, that in the relevant temperature range of the CVS reactor system, i.e. in the range between 700 and 1100 K, Zn exhibits a substantially smaller vapor pressure than Mg in order to be directly combusted at reduced oxygen pressures.
31 Hlaing Oo, W. M., M. D. McCluskey, A. D. Lalonde and M. G. Norton, *Appl. Phys. Lett.*, 2005, **86**, 7311.
32 H. Noei, C. Wöll, M. Muhler and Y. Wang, *J. Phys. Chem. C*, 2011, **115**, 908–914.
33 M. Buchholz, P. G. Weidler, F. Bebensee, A. Nefedov and C. Wöll, *Phys Chem Chem Phys*, 2014, **16**, 1672–1678.
34 S. Z. Weisz, O. Resto, G. Yaron, A. Many and Y. Goldstein, *J. Vac. Sci. Technol. A*, 1987, **5**, 302.
35 G. Spoto, E. N. Gribov, G. Ricchiardi, A. Damin, D. Scarano, S. Bordiga, C. Lamberti and A. Zecchina, *Progress in Surface Science*, 2004, **76**, 71–146.

36 A. L. Shluger, P. V. Sushko and L. N. Kantorovich, *Physical Review B - Condensed Matter and Materials Physics*, 1999, **59**, 2417–2430.
37 P. V. Sushko and A. L. Shluger, *Surface Science*, 1999, **421**, L157.
38 K. M. Beck, A. G. Joly, O. Diwald, S. Stankic, P. E. Trevisanutto, P. V. Sushko, A. L. Shluger and W. P. Hess, *Surface Science*, 2008, **602**, 1968–1973.
39 A. Sternig, S. Stankic, M. Müller, N. Siedl and O. Diwald, *Nanoscale*, 2012, **4**, 7494–7500.
40 A. Stevanovic and J. T. Yates, JR., *Langmuir*, 2012, **28**, 5652–5659.
41 Z. Zhang and J. T. Yates, *Chem. Rev.*, 2012, **112**, 5520–5551.
42 W.-C. Sun, Y.-C. Yeh, C.-T. Ko, H. He and M.-J. Chen, *Nanoscale Res Lett*, 2011, **6**, 556.
43 A. Janotti and C. G. van de Walle, *phys. stat. sol. (b)*, 2011, **248**, 799–804.
44 S. Stankic, J. Bernardi, O. Diwald and E. Knözinger, *Journal of Physical Chemistry B*, 2006, **110**, 13866–13871.
45 A. Sternig, M. Müller, M. McCallum, J. Bernardi and O. Diwald, *Small*, 2010, **6**, 582–588.
46 M. Müller, S. Stankic, O. Diwald, E. Knözinger, P. V. Sushko, P. E. Trevisanutto and A. L. Shluger, *Journal of the American Chemical Society*, 2007, **129**, 12491–12496.
47 G. L. Mar, P. Y. Timbrell and R. N. Lamb, *Chem. Mater.*, 1995, **7**, 1890–1896.
48 L. Spanhel, *J Sol-Gel Sci Technol*, 2006, **39**, 7–24.
49 Z. Li, Y. Luan, T. Mu and G. Chen, *Chem. Commun. (Camb.)*, 2009, 1258–1260.
50 M. Ghosh, R. S. Ningthoujam, R. K. Vatsa, D. Das, V. Nataraju, S. C. Gadkari, S. K. Gupta and D. Bahadur, *J. Appl. Phys.*, 2011, **110**, 54309.
51 Xiulan Hu, Y. Masuda, T. Ohji and K. Kato, in *2010 IEEE 3rd International Nanoelectronics Conference (INEC 2010)*, pp. 943–944.
52 S. Yue, Z. Yan, Y. Shi and G. Ran, *Materials Letters*, 2013, **98**, 246–249.
53 A. Kołodziejczak-Radzimska and T. Jesionowski, *Materials*, 2014, **7**, 2833–2881.
54 H. Idriss and M. A. Barteau, *Journal of Physical Chemistry*, 1992, **96**, 3382–3388.
55 H. Idriss, *J. Vac. Sci. Technol. A*, 1993, **11**, 209.
56 H. Idriss and M. A. Barteau, *Advances in Catalysis*, 2000, **45**, 261–331.
57 Y. Xia, Y. Xiong, B. Lim and S. E. Skrabalak, *Angewandte Chemie - International Edition*, 2009, **48**, 60–103.
58 D. Briggs and J. T. Grant, *Surface analysis by Auger and x-ray photoelectron spectroscopy*, IM Publications, Chichester, 2003.